Chemical Papers
https://doi.org/10.1007/s11696-021-01949-5

ORIGINAL PAPER

Crystallographic analysis of biphasic hydroxyapatite synthesized by different methods: an appraisal between new and existing models

Md. Sahadat Hossain[1] · **Monika Mahmud**[1] · **Mashrafi Bin Mobarak**[1] · **Samina Ahmed**[1,2]

Received: 22 July 2021 / Accepted: 23 October 2021

Abstract

This paper reports a detail crystallographic investigation of a well-known biphasic biomaterial containing hydroxyapatite (HAp) and β-tricalcium phosphate (β-TCP). This biphasic calcium phosphate bioceramic (BCP) was synthesized by three typical methods: (i) solid-state method (where $CaCO_3$ and $(NH4)_2HPO_4$ was the source of Ca and P, respectively); (ii) wet chemical method (where the reactants were $Ca(OH)_2$ and H_3PO_4); and (iii) direct incineration of bovine bones. Furthermore, the adopted fourth method to synthesize the biphasic biomaterial was UV irradiation instead of high temperature calcination. In each case the synthetic biphasic biomaterial was characterized by employing X-ray diffraction (XRD) and Fourier transform infrared (FT-IR) techniques. Various crystallographic parameters such as crystallite size, dislocation density, microstrain, crystallinity index (from XRD and FT-IR), HAp percentage, β-TCP percentage, the volume fraction of β-TCP, and degree of crystallinity were estimated by conventional approaches for the broader applicability of this biphasic biomaterial. Two new models for measuring microstrain and one new method (XRD-$\sin^2\Psi$ technique) for calculating residual stress (also known as intrinsic stress) were developed to estimate the crystallographic parameter more accurately. A linear relationship was illustrated among the value of conventional methods and newly developed techniques without significant difference (R^2 = more than 0.9) among the values of four types of HAp.

✉ Samina Ahmed
shanta_samina@yahoo.com

[1] Glass Research Division, Institute of Glass and Ceramic Research and Testing, Bangladesh Council of Scientific and Industrial Research (BCSIR), Dhaka 1205, Bangladesh

[2] BCSIR Laboratories Dhaka, Bangladesh Council of Scientific and Industrial Research (BCSIR), Dhaka 1205, Bangladesh

Graphical abstract

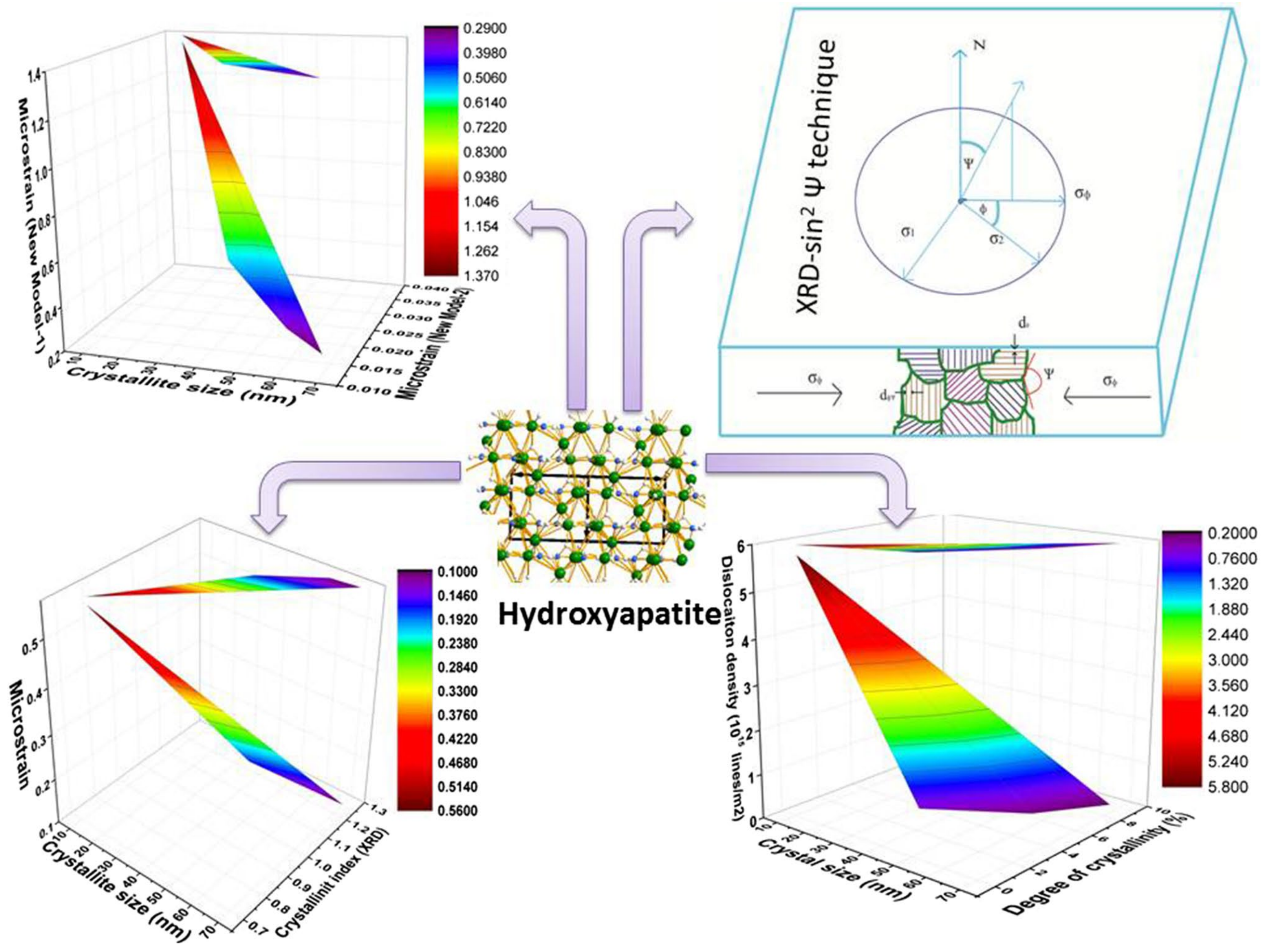

Keywords X-ray diffraction · Natural bone · Crystallite size · Residual stress · UV radiation

Introduction

Application of biomaterials in bone tissue engineering is now a fascinating area of research. In particular, Ca-phosphate-based biomaterials (BCP) are now in the top choice to be used in bone tissue engineering research. Nevertheless, hydroxyapatite (HAp) and β-tricalcium phosphate [β-TCP] having chemical formulae $Ca_{10}(PO_4)_6(OH)_2$, $Ca_3(PO_4)_2$], respectively, are the two most important candidates which attract the attention of the biomaterial researchers. HAp is a naturally occurring biomaterial (Pazarçeviren et al. 2021) responsible for 70% (by wt.) or 50% (by volume) human bone (Puad et al. 2021). It has received researcher's consideration for its non-toxic, biocompatible (Shi et al. 2021), bioactive (Awasthi et al. 2020), osteoconductive (Awasthi et al. 2020), and hemostatic nature (Gong et al. 2021). Indeed, all these properties have tagged it as a promising material for applications in various sectors such as bone tissue reconstruction (Liu et al. 2021), drug carrier (Karacan et al. 2021), bone tissue engineering, orthopedic and dental (Du et al. 2021), catalyst and catalyst carrier (Vigneshwaran et al. 2021), protein delivery (El-Fiqi and Kim 2021), gene delivery agent (Kermanian et al. 2021), water treatment (Nayak and Bhushan 2021), and antibody purification (Ghorbani et al. 2021). Generally, the structure and size of crystals govern the properties as well as the efficient applications of crystalline materials. The applications of HAp depend on the crystal size, shape, crystallinity, morphology, solubility, and defect, which are resulted from the synthesis phenomena. The raw materials, synthesis process, and reaction conditions are the vital factors, which control the crystallographic structure of HAp along with applications. Generally, HAps are synthesized from various natural sources such as eggshells (Ashokan et al. 2021), fishbone (Hernández-Cocoletzi et al. 2020) and bovine bone (Shaikh et al. 2020) by a number of techniques such as solid-state method (Javadinejad and Ebrahimi-Kahrizsangi 2021), co-precipitation (Sasaki et al. 2020), gas injection approach (Nosrati et al. 2020), emulsion, hydrolysis, sol–gel method, hydrothermal approach plasma synthesis, and microwave (Agbeboh et al. 2020).

It is well known that, owing to poor thermal stability coupled with low degradation rate as well as lightweight mechanical properties (e.g., low-impact resistance), synthetic HAp has limited its widespread applications. Conversely, pronounced biodegradability of β-TCP stimulates the formation of continuous interface between Ca-phosphate ceramics and bone. Hence, currently, biphasic calcium phosphate ceramic (BCP) consists of a mixture of HAp and β-TCP possess distinctive dissolution characteristics in supporting new bone formation at the implant-bone boundary and is considered superior when compared with either single-phase HAp or β-TCP. Concerning these facts, here we attempted to synthesize this well-known biphasic biomaterial (BCP) containing HAp and (β-TCP) by three typical methods: (i) solid-state method (where $CaCO_3$ and $(NH4)_2HPO_4$ were the source of Ca and P, respectively); (ii) wet chemical method (where the reactants were $Ca(OH)_2$ and H_3PO_4); and (iii) direct incineration of bovine bones. Furthermore, our adopted fourth method employed UV irradiation. Very recently we have developed this UV irradiation approach where HAp in biphasic form was synthesized by directly illuminating the source materials (Sultana et al. 2021) and the potency of this biomaterial was examined which was encouraging. Nevertheless, such an approach offered the advantage to synthesize the desired product at ambient temperature. Alternatively, this UV-illumination eliminated the necessity of high temperature calcination and thus revealed as an environment-friendly economic method. Because, since the production cost of any materials is associated with the reaction parameters such as temperature, pressure, and catalyst, replacement of high temperature sintering by UV irradiation will be favorable to diminish the production cost. Essentially, for any successful applications in biomedical science ranging from bone regeneration to drug delivery, the desired properties of synthetic HAp must mimic the properties of natural HAp. Hence, it is necessary to have a detailed crystallographic information in this regard which is scarce now. Concerning this point, a detailed but precise investigation has been carried out to explore the crystallographic parameters of the biphasic biomaterial. We used the existing methods together with two newly developed models and one new method (XRD-$\sin^2\Psi$ technique) for more precise calculation of microstrain and residual stress (also known as intrinsic stress), respectively.

Materials and methods

Materials

All the required chemicals were categorically analytical grade, collected from E-Merck Germany and used as received. Bovine bones were collected from a nearby shop located in Savar, Dhaka, Bangladesh, and preserved after washing with hot and double distilled water as well as deionized (after double distillation) water.

Methods

Synthesis of biphasic hydroxyapatite

In the solid-state method, keeping the ratio of Ca:P at 1.67, the chosen starting materials [$CaCO_3$ and $(NH_4)_2HPO_4$] were ball milled followed by thermal treatment. The reaction protocol consisted of ball milling at 550 rpm for 5 h and then high temperature calcination at 900 °C (soaking time 30 min and the temperature increment rate 3 °C/min). Detailed procedure is described by Samina et al. (2011) and the associated reaction is given in Eq. 1. On the other hand, the wet chemical synthesis of biphasic HAp comprised the reaction between $Ca(OH)_2$ and H_3PO_4, which were the source of Ca and P (ratio Ca/p = 1.67), respectively. However, to begin with, requisite molar solution of $Ca(OH)_2$ and H_3PO_4 (1.25 M and 5.19 M) was prepared in aqueous medium keeping a highly alkaline condition (pH 10–11). Phosphoric acid was then slowly (0.9 ml/min) added to calcium hydroxide. The alkaline environment favored the desired HAp to be precipitated in the solution which was then seasoned for 7 days with time to time stirring. During the whole course of the reaction, targeted pH was adjusted by adding ammonia solution. After 7 days the precipitate was collected and divided into two parts. One half of the precipitate was subjected to thermal treatment at 900 °C for 30 min (upraised rate of calcination temperature was 3 °C/min) which resulted the formation of desired HAp denoted by W-HAp (Eq. 2). The other half (in paste form) was exposed to UV radiation (9 h using 254 nm wavelength lamp) and the obtained HAp is expressed here as U-HAp (Eq. 3). For direct incineration, bovine bones were cleaned, boiled with distilled water and dipped in acetone for 12 h. Then, the bones were washed with copious volume of DI water and dried completely. Dried bones were then crushed into small parts and incinerated at 900 °C temperature for 30 min with an increment rate of 3 °C/min. This incineration process resulted C-HAp (Eq. 4).

Solid-state biphasic HAp:

$$10\,\mathrm{CaCO_3} + 6\left(\mathrm{NH_4}\right)_2\mathrm{HPO_4} + \xrightarrow{\text{high temp. sintering}} (1-x)\mathrm{Ca_{10}}\left(\mathrm{PO_4}\right)_2(\mathrm{OH})_2 + 3x\mathrm{Ca_3}\left(\mathrm{PO_4}\right)_2\text{Biphasic HAp(S - HAp)} \tag{1}$$

Wet chemical and UV-assisted biphasic HAp:

$$10\mathrm{Ca(OH)_2} + 6\mathrm{H_3PO_4} \xrightarrow{\text{wet chemical reaction}} \text{ppt of HAp} \xrightarrow{\text{calcination at 900°C}} \text{Biphasic HAp(W-HAp)} \tag{2}$$

$$\overset{\downarrow}{\overline{\text{UV-illumination}\longrightarrow\text{Biphasic HAp(U - HAp)}}} \tag{3}$$

Bovine bone/cow bone incinerated biphasic HAp:

$$\text{Cleaned bovine bone} \xrightarrow{\text{direct incineration at 900°C}} \text{Biphasic HAp(C - HAp)} \tag{4}$$

X-ray diffraction analysis

An X-ray diffractometer (PANalytical X'pert PRO XRD PW 3040) was used to explore the crystallographic information such as lattice parameters, crystallite size, degree of crystallinity, dislocation density, microstrain, crystallinity index, percentage of β-TCP, and the volume fraction of β-TCP of synthesized biphasic HAp. The radiation source, CuKα ($\lambda = 1.54060$), was used to record data ($2\theta = 5$–$75°$) with 0.01 steps and instrumental broadening was neglected. The machine was operated at 40 kV and 30 mA maintaining the cooling temperature at 19–20 °C. The standard JCPDS file (card no. 01-071-5048) was chosen for the comparison of synthesized data and the data were analyzed using High Score software.

FT-IR spectroscopy

The functional groups of all synthesized HAps were identified by an FT-IR machine (IR-Prestige 21, Shimadzu Corporation, Japan) comprising the attenuated total reflectance (ATR) facility. The FT-IR spectra were documented in the range of 4000–400 $\mathrm{cm^{-1}}$ wavenumber having 4 $\mathrm{cm^{-1}}$ spectral resolution.

Results and discussion

X-ray diffraction analysis

Representative XRD patterns of S-HAp, W-HAp, U-HAp, and C-HAp denoting counts/s in the Y-axis and 2-theta (degree) in the X-axis are given in Fig. 1. All the diffractograms showed the appearance of the significant peak at 31.78° (211) accompanied by two adjacent peaks at 32.26° (112) and 32.95° (300) which are distinctive of HAp formation. However, another noticeable peak at 2θ position 31.02° (0210) disclosed the presence of β-TCP as the second phase. The experimental data were compared with the standard JCPDS data (card no: 01-071-5048) and are presented in Table 1. The calculated lattice parameters (from Eq. 5) and major peaks from all four HAps coincide with the JCPDS standard. Though there are slight variations in relative intensity and peak position, Table 1 carries good evidence for the biphasic HAp phase.

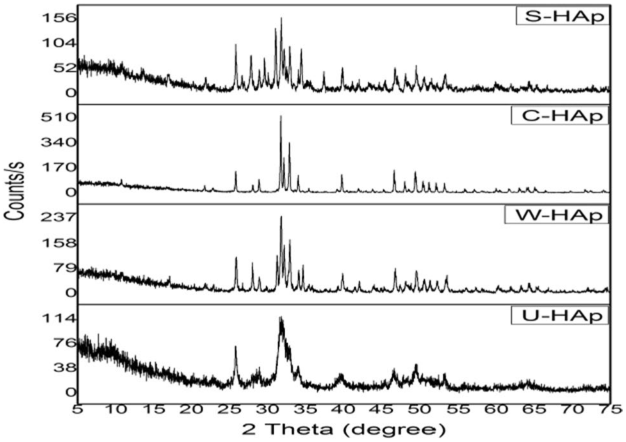

Fig. 1 X-ray diffraction of S-HAp, W-HAp, U-HAp, and C-Hap

Crystallographic parameters such as degree of crystallinity, dislocation density, microstrain, crystallinity index, HAp percentage, β-TCP percentage, and volume fraction of β-TCP are indispensable for successful applications of crystalline materials. Hence, as a consequence, the respective values were determined with the aid of Eqs. 5–13 (Sa et al. 2017; Abdel-Aal and Abdel-Rahman 2020; Rabiei et al. 2020; Pazarçeviren et al. 2021) while Table 2 represents the calculated crystallographic data of synthesized HAp samples.

$$\text{Lattice parameter equation,}\left(\frac{1}{d_{hkl}}\right)^2 = \frac{4}{3}\left(\frac{h^2+hk+k^2}{a^2}\right) + \frac{l^2}{c^2} \tag{5}$$

$$\text{Crystallite size,}\,D_c = \frac{K\lambda}{\beta\cos\theta} \tag{6}$$

$$\text{Crystallinity index, CI}_{\text{XRD}} = \sum \frac{H_{(202)} + H_{(300)}+) + H_{(112)}}{H_{(211)}} \tag{7}$$

$$\text{Degree of Crystallinity,}\,Xc = \left(\frac{Ka}{\beta}\right)^3 = \left(\frac{0.24}{\beta}\right)^3 \tag{8}$$

Table 1 Comparison of obtained and calculated data with standard JCPDS data

Standard values, lattice parameters		Experimental values and lattice parameters of the synthesized biphasic HAp								h k l
JCPDS-HAp		S-Hap		W-HAp		U-HAp		C-HAp		
d-value	Intensity %	*d*-value	Intensity	*d*-value	Intensity %	*d*-value	Intensity %	*d*-value	Intensity %	
2.815	100	2.814	100	2.813	100	2.816	100	2.818	100	2 1 1
2.779	51.90	2.780	58.96	2.779	62.52	2.776	85.00	2.783	46.97	1 1 2
2.720	61.20	2.720	67.20	2.719	70.56	2.720	55.00	2.724	65.80	3 0 0
a = b = 9.42 Å c = 6.88 Å V = 529.56 Å		a = b = 9.42 Å c = 6.89 Å V = 530.19 Å		a = b = 9.42 Å c = 6.87 Å V = 527.95 Å		a = b = 9.42 Å c = 6.89 Å V = 531.18 Å		a = b = 9.43 Å c = 6.89 Å V = 532.11 Å		
JCPDS-β-TCP		Experimental lattice parameters of the synthesized biphasic β-TCP								
		S-Hap		W-HAp		U-HAp		C-HAp		
a = b = 10.42 Å c = 37.37 Å V = 3513.79 Å		a = b = 10.46 Å c = 37.32 Å V = 3536.08 Å		a = b = 10.68 Å c = 37.08 Å V = 3662.69 Å		a = b = 10.67 Å c = 37.08 Å V = 3655.83 Å		a = b = 10.70 Å c = 37.17 Å V = 3685.34 Å		

$$\text{Dislocation density}, \delta = \frac{1}{\left(D_C\right)^2} \tag{9}$$

$$\text{Microstrain}, \varepsilon = \frac{\beta}{4 \tan \theta} \tag{10}$$

$$\text{Percentage of } \beta - \text{TCP} = \frac{I_{\beta-\text{TCP}(0210)}}{I_{\text{HA}(211)} + I_{\beta-\text{TCP}(0210)}} \tag{11}$$

$$\text{Percentage of HAp} = \frac{I_{\text{HA}(211)}}{I_{\text{HA}(211)} + I_{\beta-\text{TCP}(0210)}} \tag{12}$$

$$\text{Volume fraction of } \beta - \text{TCP}, X_B = \frac{PW_B}{1 + (P-1)W_B} \tag{13}$$

The notations of the equations are: *a/b/c* = Length of unit cell edges in *x*, *y,* and *z* direction; *h*, *k*, *l* are the Planes of unit cell; *K* is the shape factor (arbitrary constant)/Scherrer's constant = 0.94; β = FWHM (full width at half maxima) in radian, θ = diffraction angle (in degree); $H_{(hkl)}$ = peak height; K_a is a constant having the value 0.24 for most of the HAp; $I_{\beta\text{-TCP}(0210)}$ = intensity of β-TCP at (0210); $I_{\text{HA}(0210)}$ = intensity of HAp at (211); *P* = integrated intensity of HAp (211) reflection to β-TCP (0210) reflection and was assumed as 2.275; and W_B = β-TCP percentage.

As it can be seen from Table 2, the crystallite size (which often referred to as the 'Gold Standard' for crystallite materials; Barbosa et al. 2020) of the four samples varies slightly. Equation 6 which is responsible for computing crystallite size gives the corresponding values in following the order: C-HAp > S-HAp > W-HAp > U-HAp. Clearly, C-HAp tends to have slightly higher value than that obtained for the other three cases. On the other hand, U-HAp (synthesized at ambient temperature) possesses the lowest crystal size. The plausible reason for such behavior could be the effect of temperature and Majid et al. (2021) concluded that crystallite size usually increases with the increase of calcination temperature because the chance of coalescence surges by increasing temperature (Majid et al. 2021).

The crystallinity index (CI_{XRD}) is one of the significant crystallographic parameters to quantify the volume fraction of crystallinity of synthesized HAp, which indicates the perfection, average crystallite size, and ordering of a crystal (Li et al. 2007; Ren et al. 2009). Table 2 depicts the crystallinity indices of synthesized S-HAp, W-HAp, U-HAp, and C-HAp, where the values were calculated by employing Eq. 7. The highest and the lowest crystallinity index were computed from natural cow bone, and UV synthesized HAp, respectively.

Table 2 Different calculated parameters of synthesized biphasic HAps

Parameter	S-Hap	W-HAp	U-HAp	C-HAp
Crystallite size, nm				
For HAp	59.94	42.07	13.14	70.09
For β-TCP	104.77	83.84	104.69	104.82
Average crystallite size, nm (HAp + β-TCP)	82.35	62.95	58.91	87.45
Degree of crystallinity, %	5.28	1.81	0.05	8.39
Dislocation density, (10^{15} lines/m^2)	0.28	0.57	5.79	0.20
Microstrain, ε	0.12	0.17	0.56	0.10
Crystallinity index CI_{XRD}	1.24	1.12	0.74	1.25
HAp percentage	73.52	86.44	79.45	85.84
β-TCP percentage	26.48	13.56	20.55	14.16
Volume Fraction of β-TCP	1.74	1.22	0.38	2.03
Crystallinity index, $CI_{FT\text{-}IR\text{-}1}$	1.86	1.82	1.80	1.89
Crystallinity index, $CI_{FT\text{-}IR\text{-}area}$	2.84	2.62	2.49	2.82

Crystallinity is the state of materials, where composing motifs (atoms or molecules) are arranged in a regular geometric pattern (Vorokh 2018). For the applications of HAp in the biomedical sector, the degree of crystallinity is of great interest since lower crystallinity increases the water solubility as well as protein absorption (Sun et al. 2001). At the same time, the degree of crystallinity is also the indicator of stiffness, hardness, and heat resistance of HAp (Sun et al. 2001). The degree of crystallinity of prepared HAps was calculated by using Eq. 8 and documented in Table 2. U-HAp exhibited a lower degree of crystallinity, and cow bone incinerated HAp (C-HAp) gives the highest value.

Dislocation density is the concentration assessing the number of dislocation lines per unit area of surface and is directly related to crystal size (Saikiran et al. 2020). In any crystalline material, it is always objectionable because it hampers the desired properties of materials. The dislocation density was calculated with the help of Eq. 9 and given in Table 2. The microstrain or local strain is the variations in the lattice parameters in the crystalline materials, and it was computed with the help of Eq. 10 and presented in Table 2. The variation in the span of the contact place of grain results in peaks broadening, and thus the microstrain changes. When the values of crystal size decrease, the microstrain value increases. The highest microstrain values were calculated for U-HAp.

The degree of crystallinity deviates to small, and the dislocation density value moves to large, when the crystallite size (from Scherrer's equation) changes from small to large. The

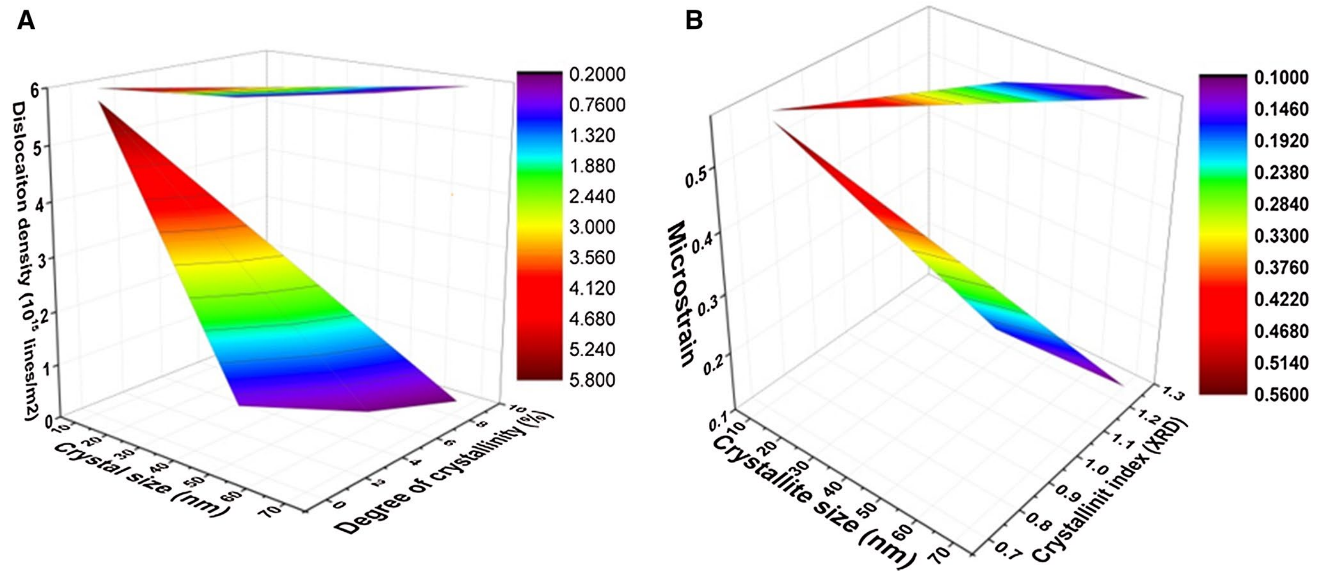

Fig. 2 Change in **A** degree of crystallinity and dislocation density and **B** microstrain and crystallinity index with crystallite size

relationship among crystallite size, degree of crystallinity, and dislocation density of synthesized HAp is clarified in Fig. 2A. If the microstrain value increases, the crystallinity index value lessens. These values also preserved a connection with crystallite size (from Scherrer's equation). The variation in values of microstrain and crystallinity index with crystallite size is illustrated in Fig. 2B.

HAp was synthesized as the main product together with β-TCP (β-Tricalcium orthophosphate). Sometimes, β-TCP is desirable for its solubility and bio-reasonability character (Sung and Kim 2003). The higher percentage of HAp indicates the efficient and favorable reaction parameters or β-TCP will be the main product. Equations 11 and 12 were employed to calculate the β-TCP and HAp percentage, and the resultant values are depicted in Table 2, where it is noticeable that if the HAp percentage increases, the β-TCP percentage decreases. Similarly, the volume fraction of β-TCP was calculated from Eq. 13 and depicted in the same table.

The major d-spacing from XRD peaks of CaO, $CaCO_3$, β-TCP, tricalcium orthophosphate hydrate, β-Calcium pyrophosphate, dicalcium orthophosphate, and dicalcium orthophosphate hydrated is 2.405, 3.043, 2.88 (or 3.4), 2.80, 3.04, 3.38, and 4.23 nm, respectively (Schlägl et al. 1987; Rehman and Bonfield 1997; Ciobanu et al. 2009; Kabir et al. 2011; Kamal and Hezma 2015). From Fig. 1, it was noticed that no significant peaks except the peak of β-TCP appeared in these regions for any HAp. The tricalcium orthophosphate hydrate, β-Calcium pyrophosphate, dicalcium orthophosphate, and dicalcium orthophosphate hydrated are formed at the higher temperature, above 1000 °C (Kamal and Hezma 2015). No such reaction conditions were associated with this research. From the XRD data, it can be assumed that the new method, applied to synthesize HAp at ambient temperature under UV radiation, completed the reaction without producing any by-product.

Crystallite size calculation using various models

Liner straight-line method of Scherrer's equation

Estimation of crystallite size is very crucial for any precise characterization and applications of crystalline material. Thus, we applied different model equations to calculate the crystallite size of HAps, which were synthesized from a newly developed method, conventional methods, and a natural source. The liner straight-line method of Scherrer's equation (LSLMSE) (Rabiei et al. 2020), which was modified from Scherrer's equation, can be employed to determine crystallite size. Equation 6 can be rearranged as follows, where DL represents the crystal size from the liner straight-line method of Scherrer's equation:

$$\cos\theta = \frac{K\lambda}{D_c} \times \frac{1}{\beta} = \frac{K\lambda}{D_L} \times \frac{1}{\beta} \tag{14}$$

Equation 14 can be compared with the liner straight-line equation as below.

$$y = mx + c \tag{15}$$

From Eq. 14, $\cos\theta$ (in degree) can be plotted in the y-axis and $\frac{1}{\beta}$ (in radian) in the *x*-axis, and the prepared graphs are illustrated in Fig. 3A for S-HAp, and supplementary Figs. a, b, and c for W-HAp, U-HAp, and C-HAp, respectively. Equations 14 and 15 can be compared to separate the slope $m=\frac{K\lambda}{D_L}$, which is used to calculate crystal size, D_L. Crystallite sizes calculated from this method are 1386.54, 693.27, 4621.80, and 1980.77 nm for S-HAp, W-HAp, U-HAp, and C-HAp, respectively. For resulting in so large crystallite size, this method is invalid for synthesized (S-HAp, W-HAp, and U-HAp) as well as natural (C-HAp) HAp.

Monshi–Scherrer method

The Monshi–Scherrer method or modified Scherrer formula, which is written in Eq. 16, can be applied to compute the crystallite size of HAp. The equation is formed after rearranging and taking 'ln' in Eq. (6) (Monshi et al. 2012). In this equation, D_M represents the crystallite size measured from Monshi–Scherrer Method.

$$\text{Monshi - Scherrer Method}, \ln\beta = \ln\frac{1}{\cos\theta} + \ln\frac{K\lambda}{D_M} \tag{16}$$

For crystallite size estimation from the Monshi–Scherrer method, $\ln\beta$, and $\ln\frac{1}{\cos\theta}$ were plotted in the y-axis, and the x-axis, respectively. The obtained graphs are represented in Fig. 3B for S-HAp, and supplementary Figs. d, e, f for W-HAp, U-HAp, and C-HAp, respectively. Comparing Eqs. 15 and 16, it can be written as below.

$$\ln\frac{K\lambda}{D_M} = \text{intercept} \tag{17}$$

Or,

$$\frac{K\lambda}{D_M} = e^{(\text{intercept})} \tag{18}$$

Taking the intercepts from Fig. s, crystallite sizes (D_M) were calculated with the help of Eq. (14). The values of crystallite size of S-HAp, W-HAp, U-HAp, and C-HAp were found 59.74, 62.93, 43.43, and 81.27 nm, respectively. These values are lower than the straight-line model in Scherrer method, and the values are very similar to the theoretical concept or values

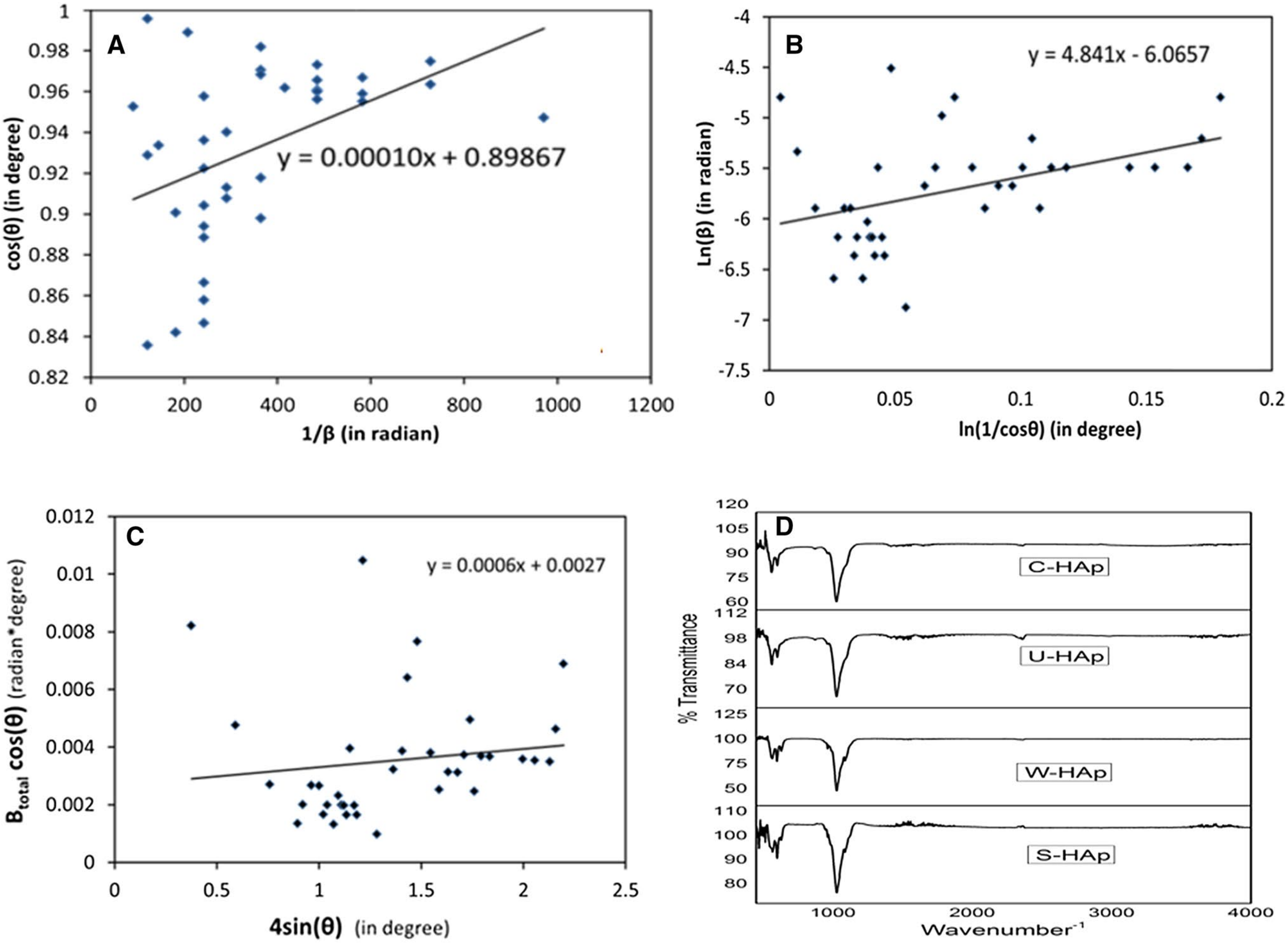

Fig. 3 Crystallite size from **A** liner straight-line method of Scherrer's equation of S-Hap, **B** Monshi–Scherrer method for S-Hap, **C** Williamson–Hall Method for S-Hap, and **D** FT-IR spectra of synthesized HAps

measured from Scherrer's formula. So, it can be assumed that the Monshi–Scherrer method is valid for the synthesized HAp.

Williamson–Hall method

The Scherrer equation and modified Scherrer equations focus only on the effect of crystallite size in XRD peak broadening without considering the intrinsic strain, which is very important in the case of nanocrystals through the grain boundaries, point defects, dislocation, and stacking (Nath et al. 2020). The Williamson–Hall method (Rabiei et al. 2020), which shows the way to calculate crystal size as well as intrinsic strain, uses the strain-induced XRD peak broadening, and the equation is given below.

$$\beta_{\text{total}} \cos\theta = \frac{K_B \lambda}{D_W} + 4\varepsilon \sin\theta \tag{19}$$

By plotting 4 sinθ (degree) in the x-axis, and β_{total} cos (radian, degree) in the y-axis, we acquired Fig. 3C for S-HAp, and supplementary Figs. g, h, and i for W-HAp, U-HAp, and C-HAp, respectively, which produced respective straight-line equation that can be compared with Eq. 11. The y-intercept, computed from the graphs, is equal to the value of $\frac{K_B \lambda}{D_w}$, which is applied to measure the crystal size (D_w). The calculated crystallite sizes of S-HAp, W-HAp, U-HAp, and C-HAp from the Williamson–Hall Method are 51, 92, 39, and 81 nm, respectively, which are within the acceptable limit. From Eq. 19, we can also calculate the intrinsic strain of the crystal by assuming ε as the slope of the straight line (Eq. 15). Thus, the slope values such as 0.0006, 0.0012, 0.0012, and 0.0002 of the respective equation represent the intrinsic strain of S-HAp, W-HAp, U-HAp, and C-HAp, respectively. As all the values are positive, the strain is called tensile strain. The strain value that emerged from the graph is very much different from that of the value estimated from Eq. (10). Equation 10 is only associated with a single angle and a peak broadening, but Eq. (19) consumed all the angles and peaks broadening.

New models for microstrain calculation

As a new approach (New Model-1) to calculate microstrain, we can rewrite Eq. 10 as below, where β is the full width at half maxima in degree.

$$4\tan\theta = \frac{\beta}{\varepsilon} = \frac{1}{\varepsilon} \times \beta \tag{20}$$

Equation (20) can be compared with the straight-line Eq. (15). By plotting β (degree) in the x-axis and 4tan θ in the y-axis, the obtained graphs and straight-line equation are illustrated in Fig. 4 for S-HAp, and supplementary Figs. j, k, and l for W-HAp, U-HAp, and C-HAp, respectively. The slopes of the equations, which are presented in the respective graph, will be equal to $\frac{1}{\varepsilon}$, and the computed microstrains are 0.35, 0.56, 1.37, and 0.29 for S-HAp, W-HAp, U-HAp, and C-HAp, respectively. The values, which are documented from this new model-1, are very much significant in comparison with the crystal size. The microstrain values showed a linear relationship with the crystal sizes (obtained from Scherrer's Equation) and are visualized in Fig. 9A. The R^2 value (above 0.9) presents no significant variation that carries good evidence for the reliability of new model-1 to calculate microstrain from this graphical method.

Indicating the same meaning as described, Eq. (20) can be rewritten as below and denoted as New Model-2.

$$4\sin(\theta) = \frac{1}{\varepsilon} \times \beta\cos(\theta) \tag{21}$$

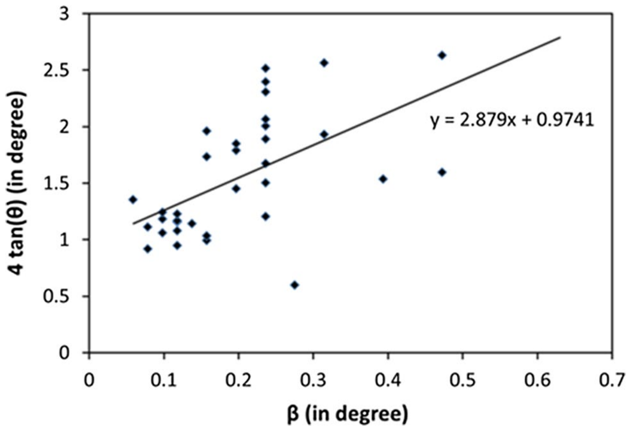

Fig. 4 New Model-1 to calculate microstrain for S-Hap

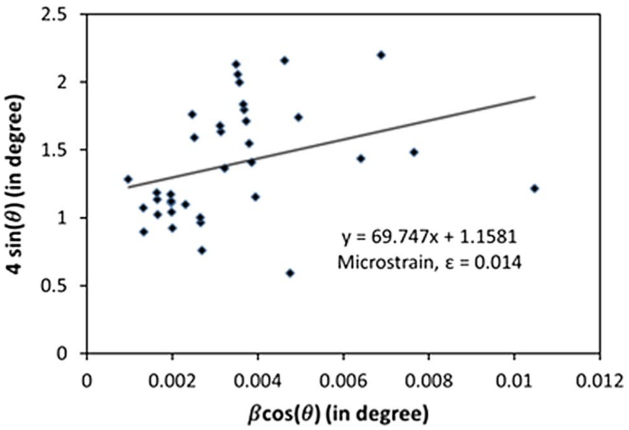

Fig. 5 New Model-2 to calculate microstrain for S-HAp

By comparing with Eq. (15), and plotting $\beta\cos(\theta)$ (degree) in the x-axis and 4 sin(θ) in the y-axis, the achieved graphs are visualized in Fig. 5 for S-HAp, and supplementary Figs. m, n, and o for W-HAp, U-HAp, and C-HAp, respectively. The measured values are 0.014, 0.018, 0.037, and 0.012 for S-HAp, W-HAp, U-HAp, and C-HAp, respectively, and demonstrate (in Fig. 9B) a linear relationship with crystal size without a notable difference ($R^2 \cong 0.9$). There were no significant variations between the values estimated from two new models of microstrain. The comparison of microstrains calculated using two new models and crystallite size measured from Scherrer's equation is pictured here in Fig. 6.

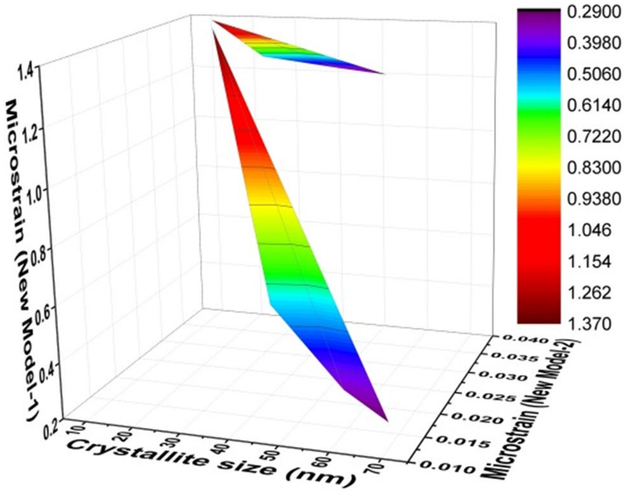

Fig. 6 Relationship among the new mode-1, new model-2, and crystallite size

The XRD-sin$^2\Psi$ technique for hydroxyapatite

For the first time, the XRD-sin$^2\Psi$ technique was used for HAp. This technique is widely applied for polycrystalline and solid materials, which are composed of numerous crystallites of different sizes and orientations. After removing external stress (extrinsic stress) from the material, the remaining stress is known as residual stress. The intrinsic stress originated in crystal because of impurities, and defects, is resulted from point defects and dislocation. A few analytical techniques are available for estimating residual stress in materials or crystals, and XRD is a unique method for such a purpose. Table 1 documents the deviation of lattice parameters from the standard JCPDS data, which originated from the residual stress of crystal deforming grain boundaries. The variation of d-spacing mainly results from the intrinsic strain and stress. For the bulk material, the intrinsic strain can be computed using the sin$^2\Psi$ method, and the respective equation is given below (Marola et al. 2021; Pandey et al. 2021).

$$\frac{d_\phi\Psi - d_0}{d_0} = \frac{1+\nu}{E} \cdot \sigma_\phi \cdot \sin^2\Psi - \frac{\nu}{E}\left(\sigma_1 + \sigma_2\right) \tag{22}$$

Equation (22) is called the principal formula for the XRD-sin$^2\Psi$ stress measurement. Figure 7 visualizes the measurement setup for HAp crystals. In this technique, E and ν are denoted as Young's modulus and Poisson's ratio at the (hkl) plane, respectively. For simplicity of explanation, stress-free lattice spacing is mentioned as d_0, and due to intrinsic stress, the lattice spacing changes to $d_{\phi\Psi}$. In the equation, σ_ϕ is the in-plane stress from two stress components (σ_1 and σ_2), and the tilt angle is Ψ, which can be measure from $\Psi = \theta - \Omega$ (glancing angle).

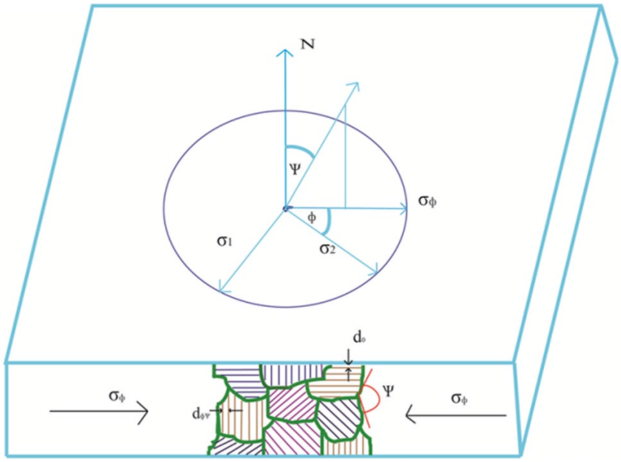

Fig. 7 Schematic diagram of XRD-sin$^2\Psi$ stress measurement in-plane stress

If in-plane stress is independent of orientation, we can write $\sigma_\phi = \sigma_1 = \sigma_2 = \sigma$ and Eq. (22) stands as below.

$$\frac{d_{\phi\Psi} - d_0}{d_0} = \frac{1+\nu}{E} \cdot \sigma \cdot \sin^2\Psi - \frac{\nu}{E}(\sigma + \sigma) \tag{23}$$

or,

$$\frac{d_{\phi\Psi} - d_0}{d_0} = \frac{1+\nu}{E} \cdot \sigma \cdot \sin^2\Psi - \frac{2\nu}{E}\sigma \tag{24}$$

or,

$$d_{\phi\Psi} = \left[\frac{1+\nu}{E} \cdot \sin^2\Psi - \frac{2\nu}{E}\right]\sigma \cdot d_0 + d_0 \tag{25}$$

By comparing Eq. (25) with straight-line Eq. (15), we can calculate the slope (σd_0), and the y-intercept (d_0). The values of E (6 GPa) and v (0.27) were taken from the literature to estimate the residual stress (Martin and Brown 1997; Charrière et al. 2001). As the lower diffraction angle produces more error, the higher angle ($30° < 2\theta > 70$) and subsequent tilt and glancing angle were considered in this method.

By plotting $[\frac{1+\nu}{E}.\sin^2\Psi - \frac{2\nu}{E}]$ in the x-axis and $d_{\phi\Psi}$ in the y-axis, the obtained graphs and respective equations (with $R^2 \cong 0.9$) are presented in Fig. 8 for S-HAp, and supplementary Figs. p, q, and r for W-HAp, U-HAp, and C-HAp, respectively. The d_0 values, which were 2.6443, 2.6553, 2.6592, and 2.6114 nm, respectively, are measured from the intercept of the equation. The residual stress was also calculated from the slope and d_0 value, and estimated as −12.17, −12.26, −13.38, and −10.84 GPa for S-HAp, W-HAp, U-HAp, and C-HAp, respectively. The negative sign is the indication of the compressive stress and the consistency of measured stress with crystallite size is illustrated in Fig. 9c maintaining $R^2 \cong 0.9$. The residual stress decreased with the increment of crystallite size and a similar pattern was noticed in the case of microstrain. Thus, the XRD-sin$^2\Psi$

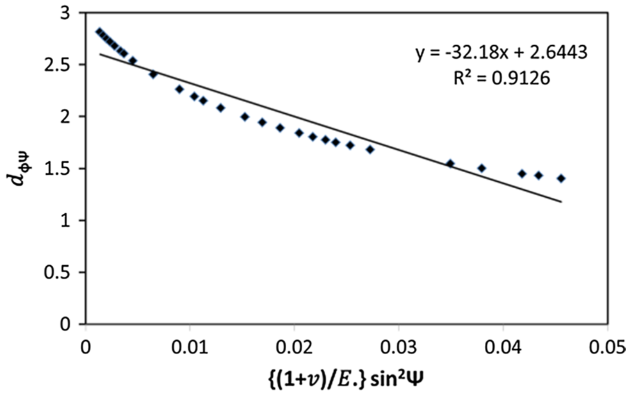

Fig. 8 XRD-sin$^2\Psi$ technique for S-HAp to calculate residual stress

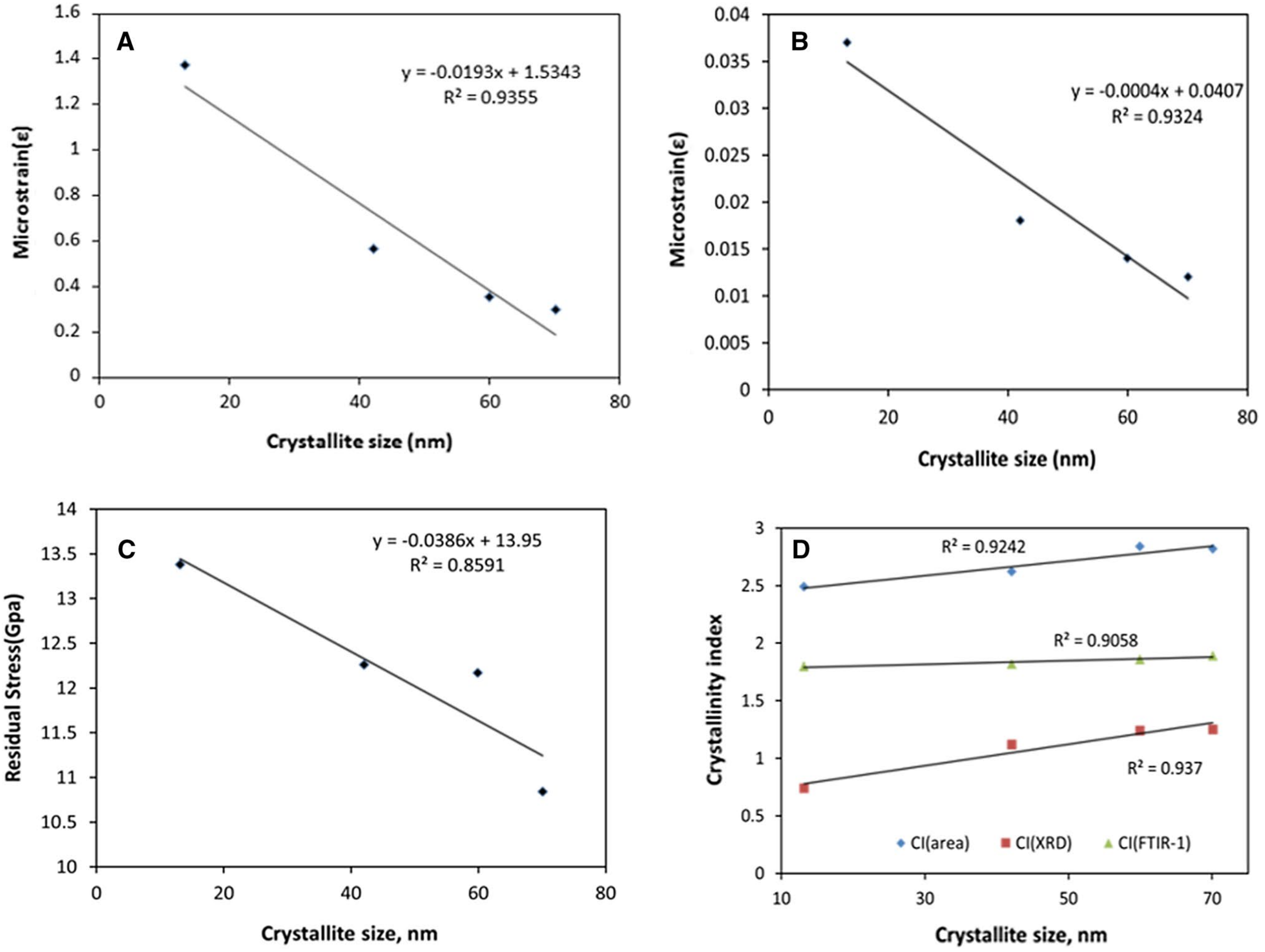

Fig. 9 Consistency between **A** crystallite size and microstrain by using New Model-1, **B** crystallite size and microstrain by using New Model-2, **C** crystallite size and residual stress by using XRD-sin$^2\Psi$ technique for hydroxyapatite, and **D** crystallite size and crystallinity index from different methods

technique can be employed for the measurement of the residual stress of HAp.

FT-IR analysis

FT-IR technique was used to identify the functional group of HAp, and Fig. 3D illustrates the spectra of synthesized HAps. The main characteristic groups present in HAp are OH^- and PO_4^{-3} along with CO_3^{-2}. The main peak of PO_4^{-3} group was found near the wavenumber of 560 cm^{-1}, 600 cm^{-1}, and 1000–1100 cm^{-1}. The peak appeared near 1030 cm^{-1} for the asymmetric stretching vibration, and the peak originated in the region of 560 cm^{-1} to 600 cm^{-1} was for the bending vibration of the phosphate group. CO_3^{-2} revealed a weak peak between 870 and 880 cm^{-1} and an intensive peak between 1460 and 1530 cm^{-1}. And, OH^{-1} exhibits a peak in the range of 3200 to 3400 cm^{-1}. These findings also supported the literature (Schlägl et al. 1987; Rehman and Bonfield 1997; Ciobanu et al. 2009). All the four HAps such as S-HAp, W-HAp, U-HAp, and C-HAp represented more or less similar peak positions in FT-IR spectra.

In the previous section of this manuscript, we calculated crystallinity index from XRD data, now FT-IR data will be taken into consideration for the same purpose. The following equation can be used to measure the crystallinity index by estimating the peak's height (Kamal and Hezma 2015)].

$$\text{Crystallinity index, CI}_{\text{FTIR - 1}} = \frac{A_{565} + A_{605}}{A_{595}} \tag{26}$$

where A_{565}, A_{605}, and A_{595} are the height of the peak at the wavenumbers of 565, 605, and 595 cm^{-1}, respectively. This region shows peaks due to the presence of the phosphate group. The higher value of the crystallinity index is responsible for the increased absorbance near 560 and 605 cm^{-1}, and decreased peak at 600 cm^{-1}. The calculated data are presented in Table 1. From this method, the highest (1.89) and the lowest (1.80) $CI_{FT\text{-}IR\text{-}1}$ were estimated for C-HAp and U-HAp, respectively.

Another equation can be applied to calculate crystallinity index and is given below (Termine and Posner 1966).

$$\text{Crystallinity index, } CI_{FTIR\text{ - }area} = \frac{A_1}{A_2} \tag{27}$$

In Eq. (27), A_2 represents the splitting area and is formed by a line joining the two splitting points near 600 cm^{-1}, and A_1 denotes the area limits sketch a baseline at the top of the band. The calculated data from Eqs. (26) and (27) are presented in Table 2. A similar trend was observed as described in the case of Eq. (26).

The crystallinity index (CI) is one of the important parameters of HAp, which is dependent on the crystallite size. Various methods, from XRD and FT-IR, were employed to estimate crystallinity index and it was tried to appraise a relationship with crystallite size measured from Scherrer's equation. The relationship between crystallite size and crystallinity index is pictured in Fig. 9D, where the R^2 values are more than 0.9 for all applied methods. In all the cases, the value of the crystallinity index was increased with the increment of crystallite size. The area-based CI from FT-IR presented relatively higher values, and XRD-based CI showed lower values. Thus, it can be assumed that all the methods applied to measure crystallinity index are significant for all synthesized HAps.

Conclusion

HAp can be synthesized from $Ca(OH)_2$ and H_3PO_4 at room temperature just applying a UV radiation source. Since no extra temperature was used in this method, small crystals were formed. The crystallographic parameters and data from the various models as well as techniques of S-HAp, W-HAp, U-HAp, and C-HAp justified the formation of HAp with identical character. The measured parameters maintained a linear relationship with the crystallite size without significant variations ($R^{2} \cong 0.9$). Microstrain estimated from the two new models also played a significant addition in the analysis of HAp. The XRD-$\sin^2\Psi$ technique can be employed to measure the residual stress of HAp, and the measured values also preserved a linear relationship with crystallite size.

Supplementary Information The online version contains supplementary material available at https://doi.org/10.1007/s11696-021-01949-5.

Author contributions MSH synthesized the hydroxyapatite samples, analyzed the data, and prepared the manuscript. MM and MBM performed FT-IR analysis. SA designed and supervised the findings of this work as well as prepared the manuscript with MSH.

Funding We gratefully acknowledge Bangladesh Council of Scientific and Industrial Research (BCSIR) authority for providing financial support regarding this research. We also acknowledge Institute of Glass and Ceramic Research and Testing (IGCRT), (BCSIR) for providing laboratory facilities and necessary supports. This research was carried out as a part of approved R&D projects of BCSIR.

Availability of data and materials All data will be made available on request according to the journal policy.

Code availability Not applicable.

Declarations

Conflict of interest There is no potential conflict of interest to describe.

Consent for publication All the authors mentioned in this manuscript agreed to publish this research work.

References

Abdel-Aal SK, Abdel-Rahman AS (2020) Graphene influence on the structure, magnetic, and optical properties of rare-earth perovskite. J Nanopart Res 22(9):1–10

Agbeboh NI, Oladele IO, Daramola OO, Adediran AA, Olasukanmi OO, Tanimola MO (2020) Environmentally sustainable processes for the synthesis of hydroxyapatite. Heliyon 6(4):e03765

Ashokan A, Rajendran V, Kumar TS, Jayaraman G (2021) Eggshell derived hydroxyapatite microspheres for chromatographic applications by a novel dissolution-precipitation method. Ceram Int 47(13):18575–18583

Awasthi S, Pandey SK, Arunan E, Srivastava C (2020) A review on hydroxyapatite coatings for the biomedical applications: experimental and theoretical perspectives. J Mater Chem B 9(2):228–249

Barbosa AA, Júnior SA, Mendes RL, de Lima RS, de Vasconcelos FA (2020) Multifunctional hydroxyapatite with potential for application in theranostic nanomedicine. Mater Sci Eng C 116:111227

Charrière E, Terrazzoni S, Pittet C, Mordasini PH, Dutoit M, Lemaıtre J, Zysset PH (2001) Mechanical characterization of brushite and hydroxyapatite cements. Biomaterials 22(21):2937–2945

Ciobanu G, Carja G, Ciobanu O, Sandu I, Sandu A (2009) SEM and EDX studies of bioactive hydroxyapatite coatings on titanium implants. Micron 40(1):143–146

Du M, Chen J, Liu K, Xing H, Song C (2021) Recent advances in biomedical engineering of nano-hydroxyapatite including dentistry, cancer treatment and bone repair. Comp B Eng 215:108790

El-Fiqi A, Kim H-W (2021) Nano/Micro-structured poly (ε-caprolactone)/gelatin nanofibers with biomimetically-grown hydroxyapatite spherules: high protein adsorption, controlled protein delivery and sustained bioactive ions release designed as a multifunctional bone regenerative membrane. Ceram Int 47(14):19873–19885

Ghorbani J, Kompany-Zareh M, Tahmasebi E (2021) Antibodies purification from human plasma using fractionation, chromatography and gel electrophoresis assisted by multivariate analysis of complimentary absorption and fluorescence spectra. J Chromatogr B 1167:122526

Gong M, Liu C, Liu C, Wang L, Shafiq F, Liu X, Sun G, Song Q, Qiao W (2021) Biomimetic hydroxyapate/polydopamine composites with good biocompatibility and efficiency for uncontrolled bleeding. J Biomed Mater Res B Appl Biomater 09(11):1876–1892

Hernández-Cocoletzi H, Salinas RA, Águila-Almanza E, Rubio-Rosas E, Chai WS, Chew KW, Mariscal-Hernández C, Show PL (2020) Natural hydroxyapatite from fishbone waste for the rapid adsorption of heavy metals of aqueous effluent. Environ Technol Innov 20:101109

Javadinejad HR, Ebrahimi-Kahrizsangi R (2021) Thermal and kinetic study of hydroxyapatite formation by solid-state reaction. Int J Chem Kinet 53(5):583–595

Kabir SF, Ahmed S, Ahsan M, Mustafa AI (2011) Investigation of sintering temperature and concentration effects on Zn substituted HA. Trends Biomater Artif Organs 25(4):154–160

Kamal H, Hezma AM (2015) Spectroscopic investigation and magnetic study of iron, manganese, copper and cobalt-doped hydroxyapatite nanopowders. Phys Sci Int J 7:137–151

Karacan I, Cox N, Dowd A, Vago R, Milthorpe B, Cazalbou S, Ben-Nissan B (2021) The synthesis of hydroxyapatite from artificially grown Red Sea hydrozoan coral for antimicrobacterial drug delivery system applications. J Aust Ceram Soc 57(2):399–407

Kermanian M, Sadighian S, Ramazani A, Naghibi M, Hosseini SH (2021) A novel mesoporous superparamagnetic hybrid silica/hydroxyapatite nanocomposite as MRI contrast agent. ChemNanoMat 7(3):284–291

Li ZY, Lam WM, Yang C, Xu B, Ni GX, Abbah SA, Cheung KMC, Luk KDK, Lu WW (2007) Chemical composition, crystal size and lattice structural changes after incorporation of strontium into biomimetic apatite. Biomaterials 28(7):1452–1460

Liu M, Shu M, Yan J, Liu X, Wang R, Hou Z, Lin J (2021) Luminescent net-like inorganic scaffolds with europium-doped hydroxyapatite for enhanced bone reconstruction. Nanoscale 13(2):1181–1194

Majid F, Shahin A, Ata S, Bibi I, Malik A, Ali A, Laref A, Iqbal M, Nazir A (2021) The effect of temperature on the structural, dielectric and magnetic properties of cobalt ferrites synthesized via hydrothermal method. Zeitschrift für Physikalische Chemie (pre published)

Marola S, Bosia S, Veltro A, Fiore G, Manfredi D, Lombardi M, Amato G, Baricco M, Battezzati L (2021) Residual stresses in additively manufactured AlSi10Mg: Raman spectroscopy and X-ray diffraction analysis. Mater Des 202:109550

Martin RI, Brown PW (1997) Phase equilibria among acid calcium phosphates. J Am Ceram Soc 80(5):1263–1266

Monshi A, Foroughi MR, Monshi MR (2012) Modified Scherrer equation to estimate more accurately nano-crystallite size using XRD. World J Nano Sci Eng 2(3):154–160

Nath D, Singh F, Das R (2020) X-ray diffraction analysis by Williamson-Hall, Halder-Wagner and size-strain plot methods of CdSe nanoparticles-a comparative study. Mater Chem Phys 239:122021

Nayak A, Bhushan B (2021) Hydroxyapatite as an advanced adsorbent for removal of heavy metal ions from water: focus on its applications and limitations. Mater Today Proc 46(20):11029–11034

Nosrati H, Mamoory RS, Le DQS, Bünger CE, Emameh RZ, Dabir F (2020) Gas injection approach for synthesis of hydroxyapatite nanorods via hydrothermal method. Mater Charact 159:110071

Pandey A, Dalal S, Dutta S, Dixit A (2021) Structural characterization of polycrystalline thin films by X-ray diffraction techniques. J Mater Sci Mater Elect 1–28

Pazarçeviren AE, Tezcaner A, Keskin D, Kolukısa ST, Sürdem S, Evis Z (2021) Boron-doped biphasic hydroxyapatite/β-tricalcium phosphate for bone tissue engineering. Biol Trace Element Res 199(3):968–980

Puad NM, Alipal J, Abdullah HZ, Idris MI, Lee TC (2021) Synthesis of eggshell derived hydroxyapatite via chemical precipitation and calcination method. Mater Today Proc 42:172–177

Rabiei M, Palevicius A, Monshi A, Nasiri S, Vilkauskas A, Janusas G (2020) Comparing methods for calculating nano crystal size of natural hydroxyapatite using X-ray diffraction. Nanomaterials 10(9):1627

Rehman I, Bonfield WJJ (1997) Characterization of hydroxyapatite and carbonated apatite by photo acoustic FTIR spectroscopy. J Mater Sci Mater Med 8(1):1–4

Ren F, Xin R, Ge X, Leng Y (2009) Characterization and structural analysis of zinc-substituted hydroxyapatites. Acta Biomater 5(8):3141–3149

Sa Y, Guo Y, Feng X, Wang M, Li P, Gao Y, Yang X, Jiang T (2017) Are different crystallinity-index-calculating methods of hydroxyapatite efficient and consistent? New J Chem 41(13):5723–5731

Saikiran A, Vivekanand M, Prahalad M, Yuvan S, Rameshbabu N (2020) Microwave synthesis of Zn/Mg substituted and Zn/Mg-F co-substituted nanocrystalline hydroxyapatite. Mater Today Proc 27:2355–2359

Samina A, Humayun MK, Farah Nigar FSK, Mustafa AI, Ahsan M (2011) Structural characterization of pure and doped calcium phosphate bioceramics prepared by simple solid state method. Sci J Commun 16–17

Sasaki K, Hayashi Y, Nakamura T, Guo B, Tian Q (2020) Stabilization of borate by hot isostatic pressing after co-precipitation with hydroxyapatite using MAP. Chemosphere 254:126860

Schlägl R, Noack K, Zbinden H, Reller A (1987) The microstructure of selective palladium hydrogenation catalysts supported on calcium carbonate and modified by lead (lindlar catalysts), studied by photoelectron spectroscopy, thermogravimetry, x-ray diffraction, and electron microscopy. Helvet Chim Acta 70(3):627–679

Shaikh MS, Husain S, Lone MA, Lone MA, Akhlaq H, Zafar MS (2020) Clinical effectiveness of anorganic bovine-derived hydroxyapatite matrix/cell-binding peptide grafts for regeneration of periodontal defects: a systematic review and meta-analysis. Regen Med 15(12):2379–2395

Shi H, Zhou Z, Li W, Fan Y, Li Z, Wei J (2021) Hydroxyapatite based materials for bone tissue engineering: a brief and comprehensive introduction. Curr Comput-Aided Drug Des 11(2):149

Sultana S, Hossain MS, Mahmud M, Mobarak MB, Kabir MH, Sharmin N, Ahmed S (2021) UV-assisted synthesis of hydroxyapatite from eggshells at ambient temperature: cytotoxicity, drug delivery and bioactivity. RSC Adv 11(6):3686–3694

Sun L, Berndt CC, Gross KA, Kucuk A (2001) Material fundamentals and clinical performance of plasma-sprayed hydroxyapatite coatings: a review. J Biomed Mater Res 58(5):570–592

Sung Y-M, Kim D-H (2003) Crystallization characteristics of yttria-stabilized zirconia/hydroxyapatite composite nanopowder. J Crystal Growth 254(3–4):411–417

Termine JD, Posner AS (1966) Infrared analysis of rat bone: age dependency of amorphous and crystalline mineral fractions. Science 153(3743):1523–1525

Vigneshwaran S, Sirajudheen P, Nabeena CP, Meenakshi S (2021) In situ fabrication of ternary TiO_2 doped grafted chitosan/hydroxyapatite nanocomposite with improved catalytic performance for the removal of organic dyes: experimental and systemic studies. Colloids Surf A Physicochem Eng Asp 611:125789

Vorokh AS (2018) Scherrer formula: estimation of error in determining small nanoparticle size. Наносистемы: физика, химия, математика 9(3)